

THE DIFFRACTION OF He ATOMS AT THE GaAs(110) SURFACE

M.J. CARDILLO, G.E. BECKER, S.J. SIBENER * and D.R. MILLER **
Bell Laboratories, Murray Hill, New Jersey 07974, USA

Received 15 October 1980; accepted for publication 16 December 1980

We present an experimental study of the diffraction of He beams at the GaAs(110) surface. Diffraction angular scans and specular intensity scans are obtained for a wide range of incident angles, azimuths, and at two energies ($\bar{E} = 0.063$ eV and $\bar{E} = 0.021$ eV). The data have been qualitatively analyzed from a classical scattering viewpoint and the hard wall eikonal scattered wave approximation. A hardwall corrugation function of the form $\zeta(x, y) = \frac{1}{2}d_x \cos(2\pi x/L_x) + \frac{1}{2}d_y \cos(2\pi y/L_y)$ yields a qualitative fit to the data with $d_x \sim 1.1$ Å and $d_y \sim 0.3$ Å, where the deep corrugation corresponds to going across the surface troughs. This value of d_x is approximately half the corrugation of the nuclear positions. Specular intensity scans are analyzed in terms of interference in the normal momentum transfer, Δk_{\perp} , which yields structural information about vertical displacements. We discuss what is required in order to appropriately describe scattering from strongly corrugated surfaces.

1. Introduction

The diffraction of He atoms from well-ordered crystalline surfaces promises to be an important tool for the study of surface structures. Although interaction energies are typically 20–100 meV with the distance of closest approach in the range of Van der Waals diameters, the diffractive scattering has been shown to be extremely sensitive to the potential contours of the outermost exposed layer of atoms [1,2]. However, at Van der Waals distances the information about the nuclear positions is indirect. For most surfaces studied to date the effective scattering potential has proven to be quite smooth, i.e. weakly corrugated. With this condition simple scattering theories are valid [3,4] and an effective hard wall potential can be readily fit to the data. However, smooth surfaces give rise to small phase shifts and the scattered intensities have little structural sensitivity. At the level of analysis accepted for smooth surfaces, it is only possible to relate the effective corrugation qualitatively to a model of the surface geometry which suggests adatom binding sites [5].

* Permanent address: James Franck Institute, University of Chicago, Chicago, Illinois 60637, USA.

** Visiting scientist from AMES Department, University of California at San Diego, La Jolla, California 92093, USA.

On the other hand if the surface potential is strongly corrugated, it may be possible to extract more definitive or direct structural information. In this case a more comprehensive level of scattering analysis is required and the interaction potential between the probe and the surface must be well understood.

The semiconductor surfaces offer an interesting prospect for the development of atom diffraction as a quantitative structural tool. All the surfaces are reconstructed from their bulk terminations and with few exceptions their geometries remain unsolved. He scattering from reconstructed silicon surfaces [1,6] has shown substantial atom diffraction intensities. The potential contours are strongly corrugated compared to most other systems studied and the scattering is associated with large phase shift variations over the unit mesh which implies detailed structural sensitivity. A central problem with diffraction analysis is the determination of a satisfactory scattering potential and its relation to the positions of the atomic cores.

We are approaching this problem by studying the scattering of He from the GaAs(110) surface. GaAs(110) is one of the few semiconductor surfaces for which the geometry seems well established [7]. Our motivation in this work is the development of a suitable description of atomic diffraction to enable us to study quantitatively other reconstructed semiconductor or strongly corrugated surfaces. The

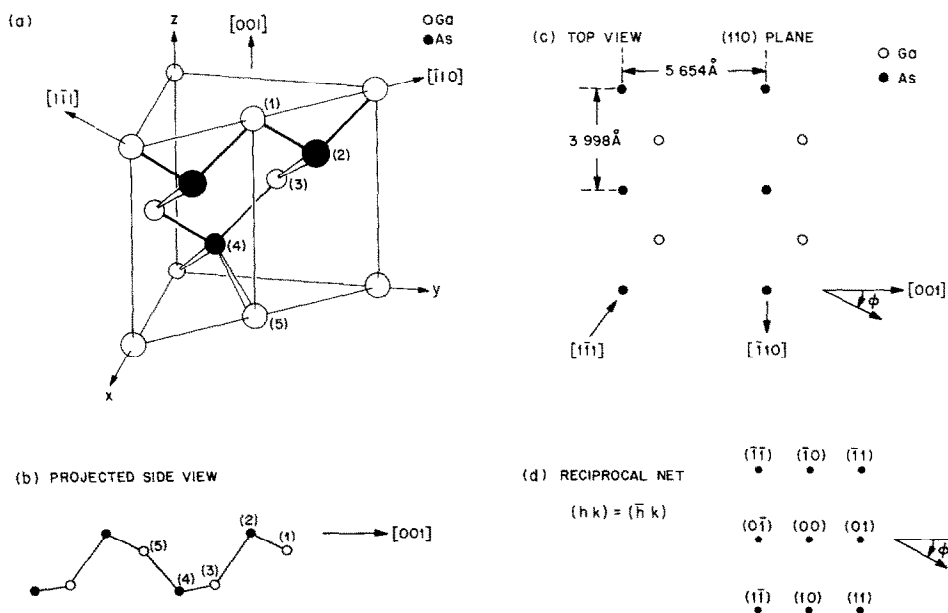


Fig. 1. GaAs crystal structure: (a) perspective of the crystal cut by a (110) plane; (b) projected side view onto the (110) plane showing the reconstruction of the top layer; (c) top view giving the surface unit mesh dimensions; (d) reciprocal net indexing and definition of ϕ .

approach is to develop a model of the He/GaAs(110) surface potential and to examine the level of scattering theory required in order to fit the “known” structure to the data. The scattering description we obtain should prove generally valuable in the analysis of atom scattering from other surfaces. In this paper we present extensive experimental data for the He/GaAs(110) system. In addition we have qualitatively analyzed the diffraction from a classical scattering viewpoint and the hard-wall eikonal scattering approximation. Although neither approach is quantitatively adequate, we can obtain qualitative fits to the data which allow us to gain physical insights into the gross shape of the surface potential. A rigorous scattering calculation for this surface is underway and will provide a more detailed understanding of He surface interaction [8].

The surface of GaAs(110) is illustrated in fig. 1 along with the conventions for angles and diffracted beams used in this paper. Note that the surface is strongly corrugated in the $\phi = 0^\circ$ direction, i.e. across the ridges and troughs, whereas it is relatively smooth parallel to the ridges and troughs, $\phi = 90^\circ$. If the surface were an unreconstructed termination of the bulk, only the small difference in atomic number for Ga and As would remove glide plane symmetry about the $\phi = 90^\circ$ direction. However, there is a surface reconstruction which consists essentially in vertical displacements of the outermost Ga and As, the result of which is a tilting of the Ga–As bond out of the horizontal plane (see fig. 1b). This reconstruction more strongly removes the scattering symmetry as is shown in the scattering patterns for the $\phi = 0^\circ$ and $\phi = 180^\circ$ directions.

2. Experimental

The apparatus has been described previously [9] and we mention here only the essential components. The incidence He beams were formed at either 300 or 100 K and have the following properties. At 300 K, $\bar{E} = 0.063$ eV, $v_{\text{mp}} = 1.75 \times 10^5$ cm/s, $\bar{\lambda} = 0.57$ Å, $\Delta v/v$ (FWHM) $\sim 8\%$. At 100 K, $\bar{E} = 0.021$ eV, $v_{\text{mp}} = 1.0 \times 10^5$ cm/s, $\bar{\lambda} = 0.98$ Å, $\Delta v/v$ (FWHM) $\sim 4\%$, where \bar{E} is the mean energy and $\bar{\lambda}$ the wavelength corresponding to the most probable velocity v_{mp} . The incident beam is square-wave modulated and the scattered beam detected by a quadrupole mass spectrometer whose output goes to a lock-in amplifier. The incident beam is collimated to 0.06° and illuminates a 1.0 mm circle at normal incidence. The detector is differentially pumped and positioned 10 cm from the crystal with double collimation for 1.5° resolution for a point source at the crystal. A point at the ionizer center views a 1.5 mm circular area at the crystal surface at normal reflection.

The scattering intensities reported below are the ratios of the lock-in amplifier output voltage for the scattered and incident beam. No corrections for beam profiles or detector view angles have been made. The view of the surface from the ionizer is well matched to the incident beam profile for most incident angles. In addition, we have measured the natural width of the scattered beams to be $\leq \frac{1}{2}^\circ$.

Thus, in most cases corrections to the diffraction intensities would be less than 10% and can be made subsequently if warranted.

The GaAs crystal is held by Ta wire to a Ta cylinder extending from a manipulator shaft at the center of a UHV chamber (2×10^{-10} Torr). The crystal can be rotated to vary the polar angle θ and the azimuth angle ϕ . It is heated by an enclosed radiation and/or electron bombardment filament from the back side. It is aligned in plane by tuning the specular beam. The crystal was cleaned by Ar^+ sputtering at 1 kV at room temperature, followed by a 5 min anneal at 970 K. This relatively high temperature was required to remove all traces of argon from the AES spectrum. A persistent contaminant was carbon. Data reported here were taken with the AES C(272)/Ga(55) ratio < 0.04 . This cleaning procedure produced a (1×1) LEED pattern with sharp spots and low background, and consistently gave the same AES spectrum and reproducible atom diffraction patterns.

The surface of the GaAs sample was shown by X-ray analysis to lie in a (110) plane within $\pm \frac{1}{2}^\circ$. The azimuthal orientation of the sample could be set approximately to a desired value by visual observation of the LEED pattern. Final precise setting of a given azimuth was done by optimizing the intensity of a He diffraction beam, such as the (03) beam in the [01] direction. The distinction between our $\phi = 0^\circ$ and 180° directions (see fig. 1) was made by a chemical etching procedure. It was found that a bromine-methanol etch produced characteristic wedge-shaped etch pits all pointing in the same direction. The wedge shape was formed by two smooth planes perpendicular to the (110) surface and meeting at an angle of $\sim 70^\circ$. (This description is most accurate for relatively small pits.) The bottom of the pit was a rather flat surface sloping down to the wedge corner. Our interpretation of this pit shape is based on the fact [10] that the etch rate for the Ga{111} planes is small compared to that for the As{111} planes. We conclude that the vertical walls of the pits are Ga{111} planes, since there are two such planes intersecting a (110) plane at right angles and forming an angle of 70.5° with each other. If, in addition, we assume that chemical etching of a {111} surface always leaves a single rather than a triple dangling bond, we conclude that the azimuth $\phi = 0^\circ$ shown in fig. 1 bisects the wedge angle and points in the same direction as does the wedge.

3. Results

In this section we present the experimental results in graphical and tabular form. In fig. 2 we plot a selected set of diffraction scans at $\lambda = 0.98 \text{ \AA}$ for two azimuths, $\phi = 0^\circ$ and $\phi = 180^\circ$, as the incident polar angle θ_i is incremented by 10° . The complete set of diffraction intensities for these azimuths at $\lambda = 0.98 \text{ \AA}$ is tabulated in table 1 and range from $30^\circ \leq \theta_i \leq 75^\circ$ for $\phi = 0^\circ$ and $30 \leq \theta_i \leq 65$ for $\phi = 180^\circ$ incremented by 5° . The noise level is too small to be shown on these plots.

Some qualitative features of fig. 2 are evident. The intense backscattering is characteristic of a strongly corrugated potential, similar to the scattering from the

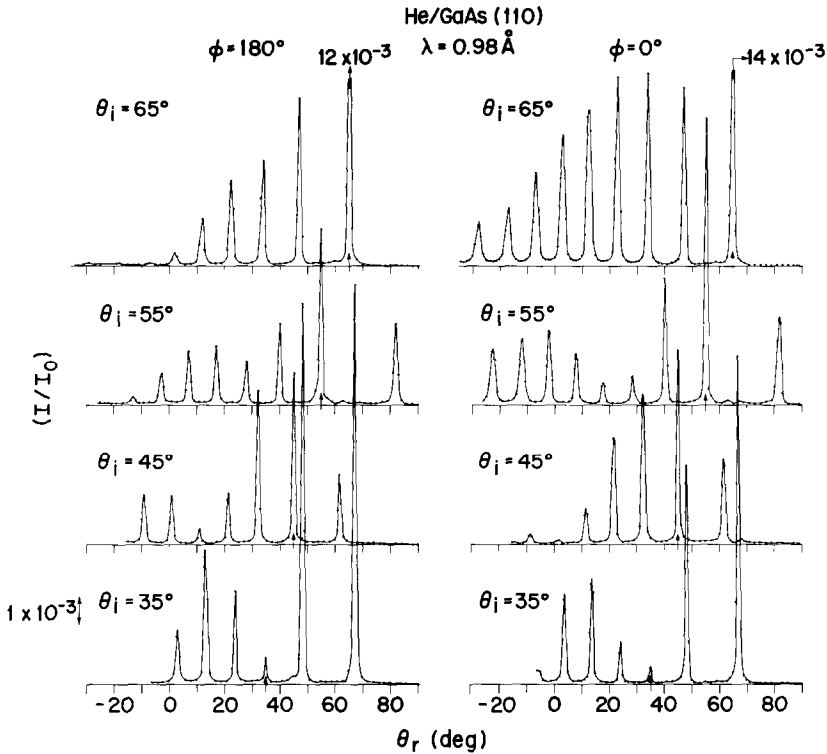


Fig. 2. Scattered signal $I(\theta_r)$ normalized to the incident beam I_0 for $\lambda = 0.98 \text{ \AA}$ at $\phi = 0^\circ$ and $\phi = 180^\circ$ for a selected set of incidence angles, θ_i (see table 1).

Si(100) surface [1]. The in-plane diffractive scattering amounts to a few percent of the incident beam. For atomic scattering, a Debye–Waller relation can be written [11] for the fractional decrease of elastic scattered intensity in a scattered beam due to thermal effects at the crystal temperature T_s ,

$$\frac{I}{I_0} = \exp \left\{ - \left[\frac{24M_g(E_i \cos^2 \theta_i + D) T_s}{M_s k_B \Theta_D^2} \right] \left[\frac{1}{4} \left(1 + \left(\frac{\cos^2 \theta_r + D/E_i}{\cos^2 \theta_i + D/E_i} \right)^{1/2} \right)^2 \right] \right\}, \quad (1)$$

where M_g and M_s are the gas and surface atom mass, k_B is the Boltzmann constant, Θ_D is the effective Debye temperature, and D is the effective attractive well depth. The second term applies to non-specular scattering. As an example, we take $D \sim 15 \text{ meV}$ and use the bulk $\Theta_D = 350 \text{ K}$ [12] at $\theta_i = 50^\circ$ to obtain $I/I_0 \sim 0.4$ for $E_i = 21.5 \text{ meV}$ and 0.2 for 63 meV. If we assume a surface Debye temperature of $\frac{2}{3}\theta_D$ we obtain 0.14 and 0.03 for these scattering ratios, respectively. Thus, although the Debye–Waller model may not be directly applicable to atom–surface scattering, we may expect approximately 10% elastic scattering for the well-ordered surface under

Table 1
 Diffraction peak amplitudes (in units of $10^{-4} I_0$): $\lambda = 0.98 \text{ \AA}$

θ_i (deg)	Beam	(05)	(08)	(07)	(06)	(05)	(04)	(03)	(02)	(01)	(00)	(01)	(02)
$\phi = 0^\circ$													
35								32	38	15	6	79	119
40							6	27	64	57	34	25	20
45						4	2	12	39	54	70	30	
50					16	12	5	3	34	93	176	99	
55				20	24	27	18	7	10	46	104	32	
60		16		22	31	43	50	54	53	51	87		
65		15		21	34	47	56	69	70	65	143		
70	7	10		16	25	39	49	65	72	71	90		
75	3	5		7	11	17	23	27	24	19	10		
$\phi = 180^\circ$													
30		(06)	(05)	(04)	(03)	(02)	(01)	(00)	(01)	(02)			
35						28	3	89	140	48			
40				2	20	49	34	10	138	144			
45				17	13	59	110	54	22	22			
50	3	11		17	6	19	56	62	25	84			
55	3	11		13	5	9	58	141	84	29			
60	5	19		45	21	16	30	64	29				
65	1	5		17	31	38	61	121					

these conditions. The fraction of the in-plane scattering that will be elastic at $\lambda = 0.98 \text{ \AA}$ can be estimated from our eikonal calculations (described subsequently) and is consistent with this Debye–Waller attenuation.

As noted earlier an important feature of the surface structure which is manifest in the data is the asymmetry between the $\phi = 0^\circ$ and 180° directions. In fig. 2 the asymmetry is readily apparent as θ_i increases towards grazing incidence. The envelopes of diffraction peaks for both azimuths consist of broad maxima which move in towards the specular beam as θ_i increases. At $\theta_i = 65^\circ$ the envelope maxima appear to coalesce with the specular beam. The inner and outer maxima will be subsequently identified as supernumerary and rainbow maxima, respectively. The lack of a symmetry plane is clearly evident in the rainbow maxima for $\theta_i = 55^\circ$ where, for $\phi = 180^\circ$, the rainbow maximum at $\theta_r = +12^\circ$ is closer to specular ($\Delta\theta_{rb} = \theta_i - \theta_{rb} \cong 43^\circ$) and of lower intensity than that for $\phi = 0^\circ$ ($\Delta\theta_{rb} \cong 60^\circ$).

The small bumps between the diffracted beams (e.g., $\phi = 0^\circ$, $\theta_i = 55^\circ$, $\theta_r = 63\text{--}68^\circ$) are reproducible and are related to inelastic events [13]. They occur for all θ_i and ϕ at $\lambda = 0.57 \text{ \AA}$ and 0.98 \AA and appear most frequently in the forward scattering directions.

In fig. 3 we present selected results for $\lambda = 0.57 \text{ \AA}$ again for $\phi = 0^\circ$ and $\phi = 180^\circ$ at increments in θ_i of 10° . A complete tabulation of the diffraction intensities recorded is given in table 2. The contraction of reciprocal space at this shorter wavelength, plus the greater percentage spread in the incident beam wavelength, result in less resolved spectra. Beams far from specular have become indistinct. The in-plane diffraction intensities for $\lambda = 0.57 \text{ \AA}$ are substantially less than for $\lambda = 0.98 \text{ \AA}$ as expected from the incident energy dependence of the Debye–Waller factor. At more normal incidence these data show less symmetry than those at $\lambda = 0.98 \text{ \AA}$. However, near $\theta_i = 50^\circ$, the envelopes show broad rainbow maxima displaced between 50° and 70° from specular. For $\phi = 180^\circ$, $\theta_i = 50^\circ$, $\Delta\theta_{rb} \sim 52^\circ$ and for $\phi = 0^\circ$, $\theta_i \cong 55^\circ$ (table 2), $\Delta\theta_{rb} \sim 70^\circ$ similar to the case for $\lambda = 0.98 \text{ \AA}$. As in fig. 2, the maxima in the envelope of beam intensities coalesce as θ_i approaches grazing incidence.

In fig. 4 we plot the results of scanning in the $\phi = 90^\circ$ direction at $\lambda = 0.98 \text{ \AA}$. The intense beams are those closest to the specular beam and are of somewhat greater amplitude than for $\phi = 0^\circ$ or 180° , indicating that the surface is effectively smoother in the $\phi = 90^\circ$ direction. A similar plot for $\lambda = 0.57 \text{ \AA}$ is given in fig. 5 and we note the greatly reduced in-plane diffraction intensity for this energy. This reduction in diffracted intensities is greater than expected from the Debye–Waller factor.

In fig. 6 we complete the presentation of diffraction results at $\phi = 305^\circ$ corresponding to the $[\bar{1}1]$ direction for $\lambda = 0.98 \text{ \AA}$. Note the similarity in the envelopes of the diffraction beams of fig. 4 and fig. 6 for $\theta_i = 30^\circ\text{--}50^\circ$. In each case there is a maximum displaced between one and two beams from specular. However, for the $[\bar{1}1]$ direction at $\theta_i = 60^\circ$ the maximum has coalesced with the specular beam.

An interesting feature of the diffraction scans is the rapid variation of the spec-

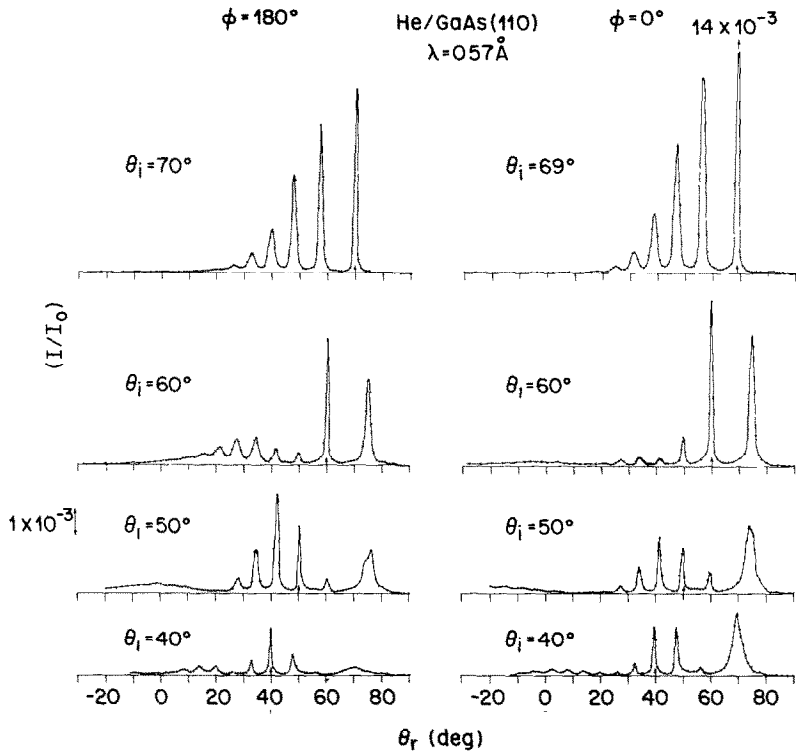


Fig. 3. Scattered signal $I(\theta_r)$ normalized to I_0 for $\lambda = 0.57 \text{ \AA}$ at $\phi = 0^\circ$ and $\phi = 180^\circ$ for a selected set of θ_i (see table 2).

ular intensity with incident angle. This variation is examined in detail in figs. 7–11 in which the specular intensity is plotted versus incident polar angle, θ_i , at different azimuths. In fig. 7 specular intensity scans are plotted for a series of 4 azimuths within 15° of the $[01]$ ($\phi = 0^\circ$) direction for $\lambda = 0.98 \text{ \AA}$. Fig. 8 is a similar plot for the $[0\bar{1}]$ ($\phi = 180^\circ$) direction for a series of 4 azimuths more closely spaced. In fig. 9 three azimuths near the $[\bar{1}\bar{2}]$ direction and one scan along the $[\bar{1}1]$ direction are included for $\lambda = 0.98 \text{ \AA}$. All of these scans show high frequency extrema characteristic of bound state resonances and broad undulations which we believe are characteristic of interference in $\Delta k_1 = (4\pi/\lambda) (\cos \theta_i)$. Interference of this nature can only be observed for highly corrugated surfaces which give rise to large phase shifts as θ_i is varied. In this paper we do not report on the fitting of bound states, but focus on the envelopes of these scans which may be directly interpretable in terms of geometric structure. Each of the 12 scans of figs. 7–9 shows a broad maximum centered between $24^\circ < \theta_i < 26^\circ$ and a sharper maximum around $\theta_i = 68^\circ$. In addition, a peak near $\theta_i = 46^\circ$ can be identified in most spectra whereas the inten-

Table 2
 Diffraction peak amplitudes (in units of $10^{-4} I_0$): $\lambda = 0.57 \text{ \AA}$ and $\phi = 0^\circ$

θ_i (deg)	Beam													
	(07)	(06)	(05)	(04)	(03)	(02)	(01)	(00)	(01)	(02)	(03)	(04)	(03)	(04)
30				1	2	2	1	1	1	5	6	3	3	14
35						1	3	4	4	3	18	14	14	6
40	1	2	2	2	1	1	4	18	18	18	3	3	22	
45			1	1	2	3	3	11	46	36	36			
50					2	9	21	17	8	25				
55					2	10	44	88	41					
60			1	2	3	3	11	60	48					
65			3	9	18	22	18	77	11					
69			3	9	22	47	72	139						
75			4	11	27	55	83	64						

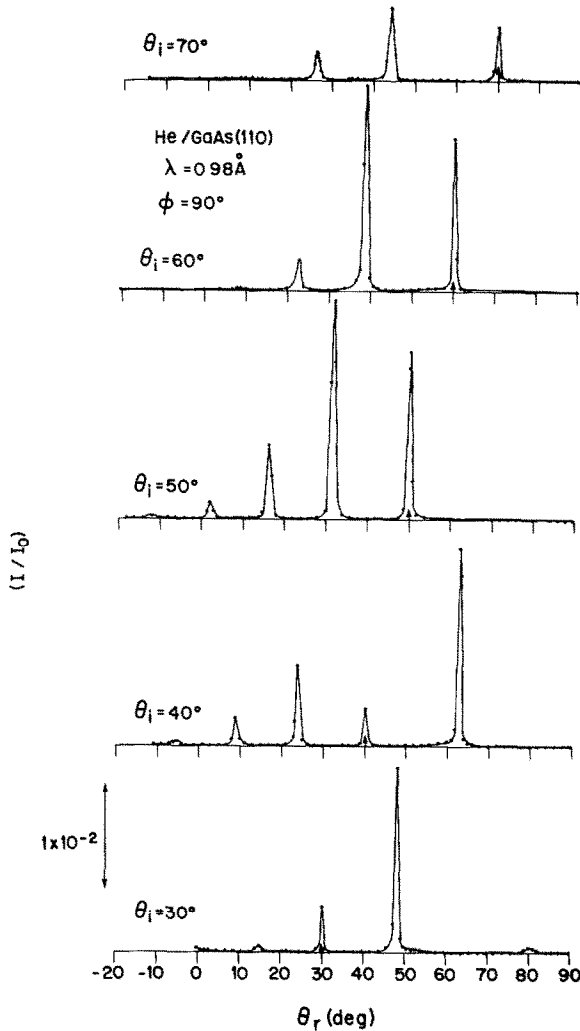


Fig. 4. Scattered signal $I(\theta_r)$ normalized to I_0 for $\lambda = 0.98 \text{ \AA}$ at $\phi = 90^\circ$ for a sequence of θ_i .

sity scattered into the region around $\theta_i = 58^\circ$ varies strongly with azimuth. Most of these spectra have similar overall contours in agreement with the simpler scattering theories in the literature [3,4]. However, in fig. 10, a very different envelope is observed in the specular scan for the [10] direction ($\phi = 90^\circ$) at $\lambda = 0.98 \text{ \AA}$, which consists of one broad maximum centered at $\theta_i = 56^\circ$. Also plotted in fig. 10 are two other scans at wavelengths of 0.90 and 0.57 \AA for the same direction. In fig. 11 we compare the high energy scan of fig. 10 along the [10] direction with a scan in the

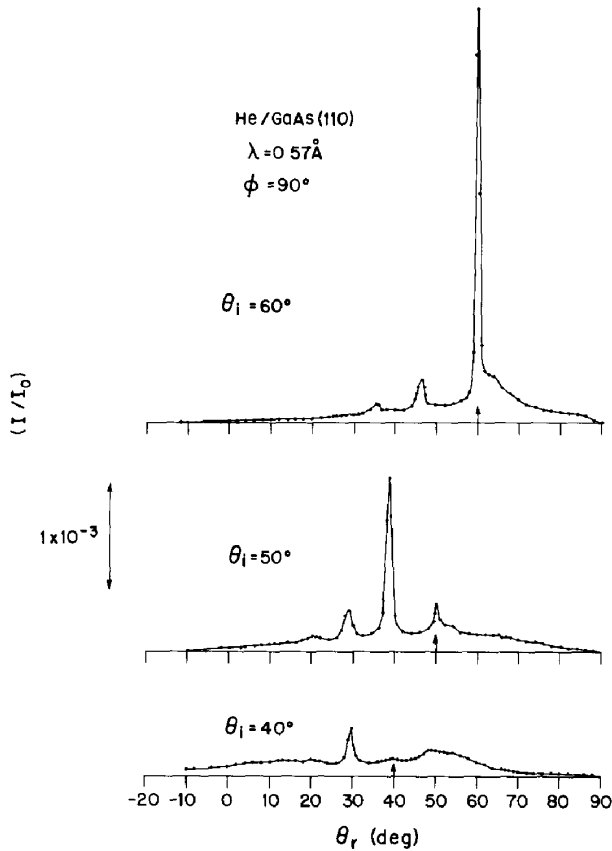


Fig. 5. Scattered signal $I(\theta_r)$ normalized to I_0 for $\lambda = 0.57 \text{ \AA}$ at $\phi = 90^\circ$ for $\theta_i = 40^\circ, 50^\circ, 60^\circ$.

[01] direction also at $\lambda = 0.57 \text{ \AA}$. Note that the higher density of reciprocal lattice rods and the broader wavelength distribution appropriate to fig. 11 causes the resonance structure to be washed out and results in smooth contours for $\theta_i \leq 60^\circ$ as compared to figs. 7–10.

4. Analysis and discussion

In this section we present a qualitative analysis of the data using simple classical scattering concepts and the eikonal scattered wave approximation. We do not expect this level of fitting to be adequate for a structural study of this surface. Rigorous scattering calculations using realistic interaction potentials [8] indicate that an adequate fit to these data requires accurate modeling of the potential and a

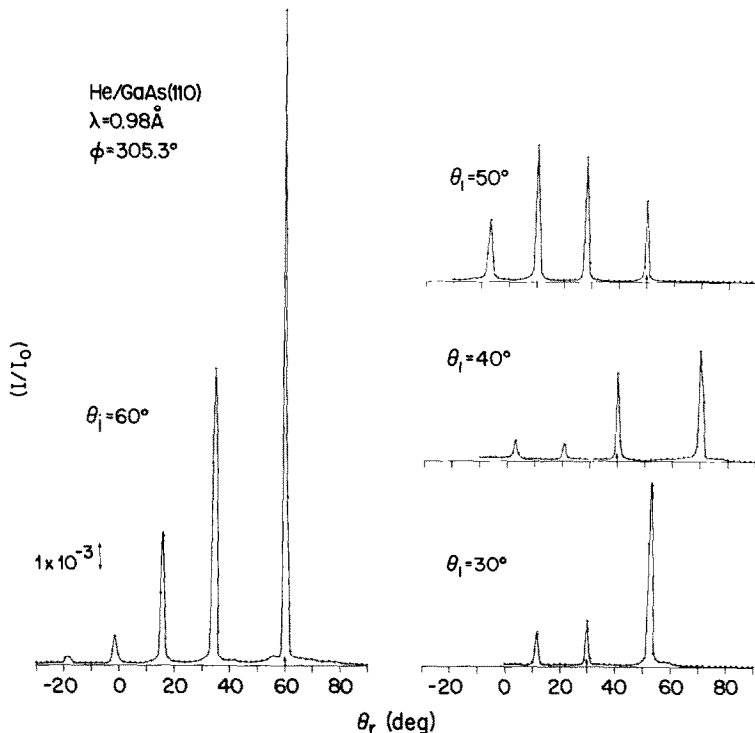


Fig. 6. Scattered signal $I(\theta_r)$ normalized to I_0 for $\lambda = 0.98 \text{ \AA}$ at $\phi = 305.3^\circ$ for a sequence of θ_i .

complete scattering theory. However, the direction of approach for complex calculations can be usefully guided by the simple qualitative analysis presented here. In addition, useful qualitative features of the potential and scattering dynamics can more easily be examined with the simple calculations.

4.1. Classical scattering

We begin our analysis of the diffraction data by interpreting the envelope maxima of figs. 2–5 from a classical rainbow scattering point of view. A comparison of the extent of backscattering in figs. 2 and 4 or figs. 3 and 5 suggest that the surface is strongly corrugated in the [01] direction, across the troughs, and weakly corrugated in the [10] direction, along the troughs, as is expected from the positions of the nuclei (fig. 1). A useful start is to characterize the magnitude of the corrugation in each direction. For the [10] direction we refer to fig. 2 where at $\theta_i = 35^\circ$ for $\phi = 0^\circ$ and 180° we observe envelope maxima displaced $\sim 25^\circ$ from specular. For $\theta_i = 45^\circ$ ($\phi = 180^\circ$) and $\theta_i = 55^\circ$ ($\phi = 0^\circ$) the displacements of the maxima are $\sim 55^\circ$ and $\sim 60^\circ$ respectively. We will assume that the envelope maxima are

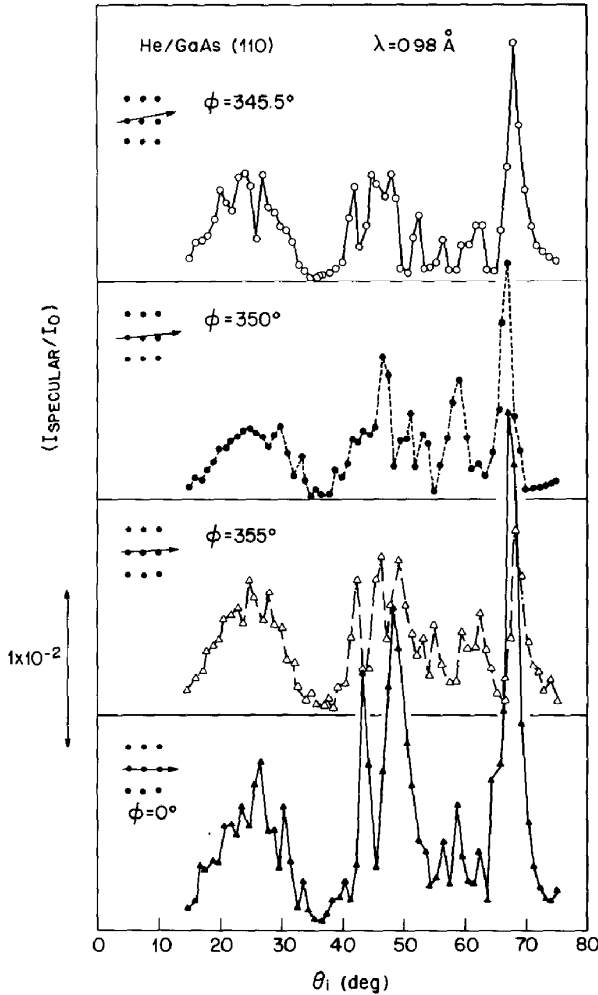


Fig. 7. Normalized specular intensity versus θ_i at $\lambda = 0.98 \text{ \AA}$ for a series of azimuths as indicated near the $\phi = 0^\circ$ direction.

described by classical rainbow scattering. Rainbows are maxima in the classical differential cross section arising from points of inflection in the scattering potential in analogy with optical rainbows. Garibaldi et al. [3] have shown that rainbow scattering has a strong quantum correspondence which suggests that the maxima can be qualitatively analyzed classically. A strictly wave-like feature of rainbow scattering, however, is the supernumerary rainbow which may occur between the rainbow maximum and the specular beam for strongly corrugated surfaces. It arises when the phase shift between trajectories with the same scattering angle but from

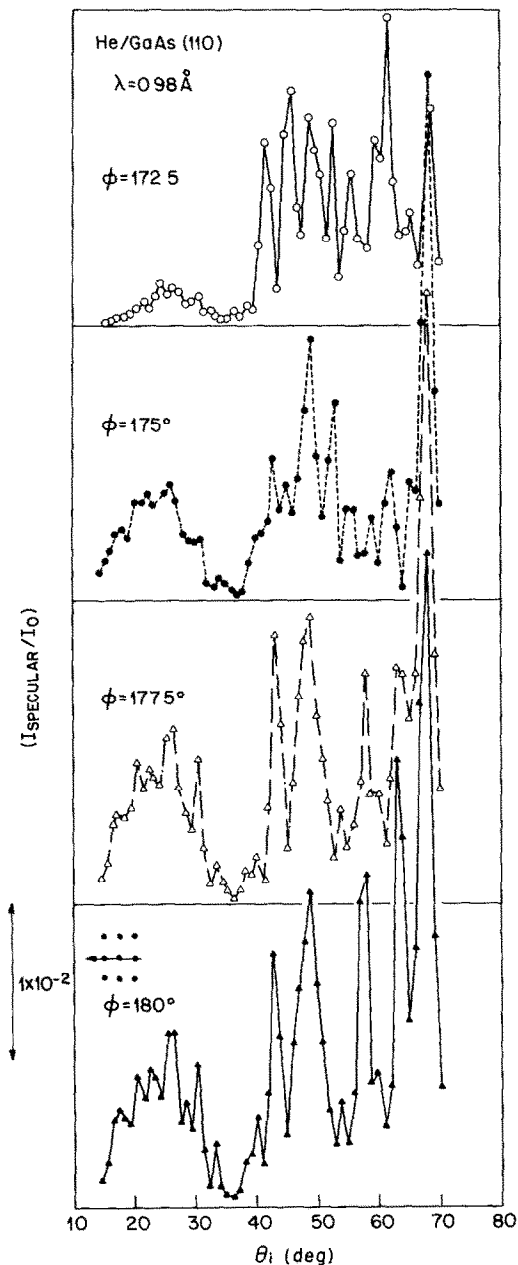


Fig. 8. Normalized specular intensity versus θ_i at $\lambda = 0.98 \text{ \AA}$ for azimuths near $\phi = 180^\circ$.

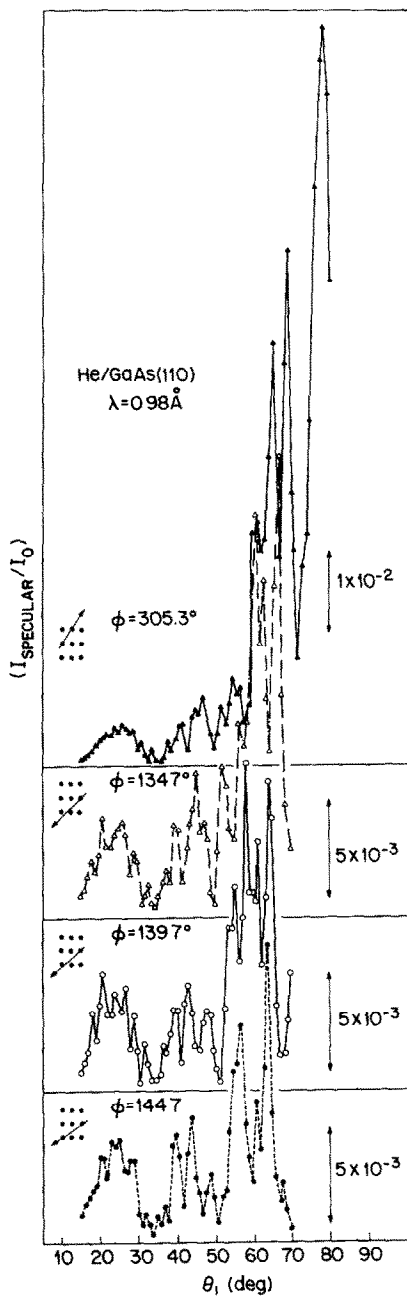


Fig. 9. Normalized specular intensity versus θ_i at $\lambda = 0.98 \text{ \AA}$ for three azimuths near the $[1\bar{1}2]$ direction and one along the $[\bar{1}11]$ direction.

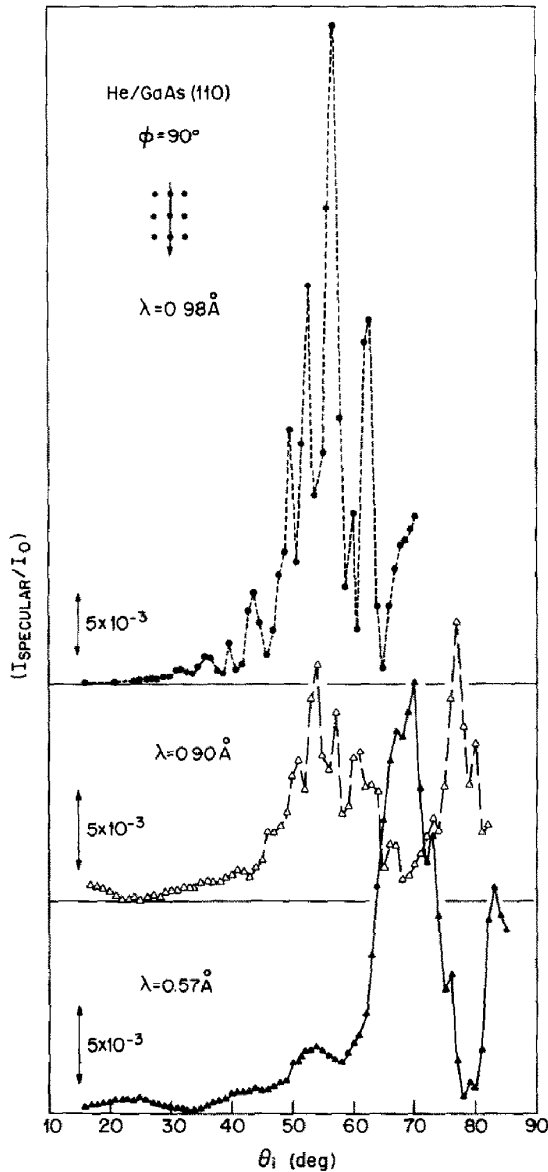


Fig. 10. Normalized specular intensity versus θ_i at $\phi = 90^\circ$ for three wavelengths.

different impact parameters within the unit net approaches 2π .

We start by assuming that the inner and outer maxima observed as θ_i is varied for either $\phi = 0$ or $\phi = 180^\circ$ are both rainbows and arise from two one-dimensional cuts across the tops of the Ga and As atoms from where we may expect in-plane

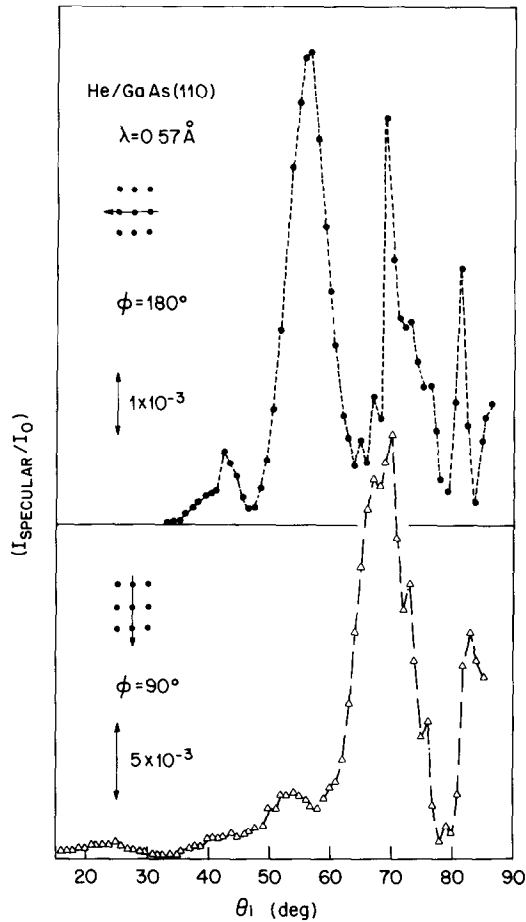


Fig. 11. Normalized specular intensity versus θ_i at $\lambda = 0.57 \text{ \AA}$ for $\phi = 90^\circ$ and $\phi = 180^\circ$.

scattering. The diffraction envelope corresponds to the classical cross section for specular scattering from a hard wall whose shape is described by the corrugation function $\zeta(x, y)$. It is straightforward to show [14] that the rainbow maximum arises from the point of inflection $d^2\zeta(x, y)/dx^2 \equiv \zeta''_{xx}(x, y) = 0$ and that a maximum occurs at a scattering angle corresponding to the slope $\zeta'_x(x, y)$ at the inflection point. Thus the angular displacement of the rainbow maximum from specular is

$$\Delta\theta_{rb} = \theta_r - \theta_i = -2 \tan^{-1} \zeta'_x(x, y). \quad (2)$$

For a periodic hard wall in one dimension of the form $\zeta(x) = \frac{1}{2}d \cos(2\pi x/L)$,

$$d = (L/\pi) \tan(\Delta\theta_{rb}/2), \quad (3)$$

and we obtain $d_1 = 0.4 \text{ \AA}$ for $\theta_i = 35^\circ$ and $d_2 = 0.9\text{--}1.0 \text{ \AA}$ for $\theta_i = 55^\circ$ where $L_x = 5.654 \text{ \AA}$.

For $\phi = 90^\circ$ (fig. 4) there is one maximum occurring approximately at $\Delta\theta_{rb} \sim 20^\circ$. For $L_y = 4.0 \text{ \AA}$ this yields an effective $d_y \sim 0.2 \text{ \AA}$ using a cosine corrugation function.

At higher energy, $\bar{E} = 0.063 \text{ eV}$, $\lambda = 0.57 \text{ \AA}$, maxima are observed at similar values of $\Delta\theta_{rb}$. This is consistent with the interpretation of rainbow maxima whose angular positions are energy independent except for refraction effects. For $\phi = 0^\circ$ and 180° , we use the weak maxima of $\theta_i = 55^\circ$ (table 2) and 50° respectively to obtain $d_x = 0.9\text{--}1.1 \text{ \AA}$. However no maximum around $\theta_r = 35^\circ$ appears consistently which suggests that this is a supernumerary feature at $\lambda = 0.98 \text{ \AA}$. In summary, hard wall classical scattering for $\theta_i \leq 55^\circ$ indicates a principal corrugation in the He surface potential of about 1.0 \AA across the troughs, which is just half of the corrugation based on nuclear positions. Parallel to the troughs the surface appears smooth with a corrugation about 0.2 \AA . These results are consistent for $\lambda = 0.98 \text{ \AA}$ and $\lambda = 0.57 \text{ \AA}$. The occurrence of a second rainbow at $\Delta\theta_{rb} = 35^\circ$ for $\lambda = 0.98 \text{ \AA}$ is not confirmed at $\lambda = 0.57 \text{ \AA}$.

The rainbow features in figs. 2 and 3 do not move in accordance with classical predictions as θ_i changes. From eq. (2), $\Delta\theta_{rb}$ should remain constant as θ_i varies. If a uniform attractive well is attached to the hard wall, $\Delta\theta_{rb}$ should increase with θ_i . As θ_i increases towards grazing incidence, the maxima in diffraction envelopes all move closer to the specular angle and eventually yield a smoothly decreasing pattern away from grazing scattering angles. By computing classical trajectories we have examined whether this coalescence of the rainbow with the specular beam may also be associated with shadowing or cut-offs. In fig. 12 we have drawn the

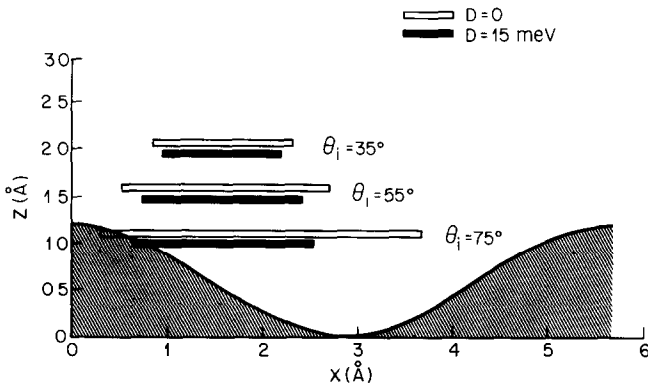


Fig. 12. Plot of the corrugation function $z(x) = 0.6 \cos(2\pi x/5.654)$ with three sets of bars for the incidence angles indicated showing the range of impact parameters for which classical trajectories to and from the surface would be shadowed or cut off. The two values of D correspond to zero attractive potential and a uniform potential of depth $D = 15 \text{ meV}$ extending beyond the range of the corrugation.

one-dimensional corrugation function corresponding to the outer rainbow at $\theta_1 = 55^\circ$, $\lambda = 0.98 \text{ \AA}$, $\phi = 0^\circ$, i.e. $\zeta(x) = 0.6 \cos(2\pi x/5.654)$. We have indicated the regions which would be shadowed and/or cut off for three cases; $\theta_1 = 35^\circ, 55^\circ, 75^\circ$. We have also included the effect of a uniform attractive potential of depth $D = 15 \text{ meV}$. The region near $x = 4.2 \text{ \AA}$, where $\zeta''(x) = 0$, is the classical origin of the backscattered rainbow. Scattering from this region is not quite cut off even at $\theta_1 = 75^\circ$ for $D = 15 \text{ meV}$. However, the extent of the surface which contributes to single scattering is diminished and the surface is effectively smoothed as the incident beam moves away from the surface normal and as the well depth increases. Thus classical shadowing and cut-offs do not directly reveal the origin of the coalescence of the envelope of diffracted intensities in figs. 2 and 4 although from the correspondence of the classical differential cross section and the quantum interference pattern they suggest that the smoothing of the effective scattering surface plays an important role.

4.2. Eikonal approximation

As an alternative description of the scattering we have used the eikonal wave scattering analysis. The eikonal solution to scattering from a hard corrugated wall (HCW) is simple although not accurate. It has been shown, using simple corrugation functions, that the HCW eikonal solution is not reliable for $d/L > 0.14$ [15]. In the [01] direction $L_x = 5.654 \text{ \AA}$ so that $d < 0.8 \text{ \AA}$ if the calculation is to be reliable and if the potential is well approximated by a hard wall. For this surface $d > 0.8 \text{ \AA}$ so that we expect the following analysis to be only qualitatively useful. We have followed the formulation of Garibaldi et al. [3] and have used their equations (2.13), (2.24), and (B20) for the in-plane diffraction intensities:

$$\frac{I_G}{I_0} = \frac{\cos \theta_G}{\cos \theta_1} \left[\frac{1 + \cos \theta_1 \cos \theta_G}{\cos \theta_G (\cos \theta_1 + \cos \theta_G)} \right]^2 \times \left[\frac{1}{L_x L_y} \int_0^{L_y} \int_0^{L_x} \exp[i\mathbf{G} \cdot \mathbf{R} + iq_{GZ}\zeta(x, y)] dx dy \right]^2, \quad (4)$$

where $q_{GZ} = (\mathbf{k}_i - \mathbf{k}_G) \cdot \hat{z} = k(\cos \theta_1 - \cos \theta_G)$ is the normal momentum transfer for diffraction, \mathbf{G} is the reciprocal lattice vector, and \mathbf{R} is a vector in the plane. In our analysis we have integrated in the real (x, y) domain for various $\zeta(x, y)$. If $\zeta(x, y)$ is separable, then the integral is simply a product of one-dimensional integrals. In one dimension for $\zeta(x) = \frac{1}{2}d \cos(2\pi x/L_x)$, the result is a Bessel function. Note that the eikonal approximation to the HCW model neglects multiple scattering, i.e. off-diagonal coupling terms in the scattering matrix. One result of the eikonal approximation is that there is no specular intensity dependence on azimuth in clear disagreement with the data of figs. 7–10.

We have tried a range of corrugation functions and discuss two models here, the

simplest and most complex. The simplest case has a glide plane through $\phi = 90^\circ$ and is written

$$\zeta(x, y) = \frac{1}{2}d_x \cos(2\pi x/L_x) + \frac{1}{2}d_y \cos(2\pi y/L_y). \quad (5)$$

In fig. 13 we plot the results for the diffraction for $d_x = 1.2 \text{ \AA}$ and $d_y = 0.36 \text{ \AA}$, which are close to the parameters suggested by the classical analysis. For $\theta_i = 35^\circ$, 45° , and 55° the backscattering envelopes are in qualitative agreement with the data of fig. 2. The maxima occur where the classical rainbows should appear for this corrugation function. The magnitude of the forward intensities are considerably off where the eikonal calculation is not expected to do well. The inner maximum observed at $\theta_i = 35^\circ$ is reproduced in this calculation and is confirmed as a super-numerary rainbow as the corrugation function does not have a second point of inflection corresponding to this angle. Note that at $\theta_i = 65^\circ$ the extrema have not coalesced in the calculations. We were unable to obtain a significant improvement over this fit with the addition of a uniform attractive well and the inclusion of a slight asymmetry in the potential. The potential is separable in x and y so that the data for $\phi = 90^\circ$ may be fit independent of the corrugation for $\phi = 0^\circ$. The y corrugation term in eq. (5) gives rise to a rainbow maximum displaced between one and two beams from specular for $\theta_i < 55^\circ$ in agreement with fig. 4. At more grazing incidence the calculation indicates the rainbow maximum collapses into the specular whereas the data do not.

In the $\phi = 305^\circ$ direction both the x and y corrugations enter and the calculations appear to fit the data of fig. 6 qualitatively well. At $\theta_i = 35^\circ$, there are maxima on each side of specular between one and two beams removed. As θ_i approaches grazing incidence the maxima collapse into the specular.

Our second model consists of a more complex hard wall corrugation and was obtained by summing contributions from nearest neighbors at each point (x, y) within the unit cell assuming this would be related to the repulsive wall. We affixed Gaussian functions to 13 lattice sites and summed as follows:

$$\zeta(\mathbf{R}) = \sum_{i=1}^{13} a_i \exp(-W_i|\mathbf{R} - \mathbf{R}_i|^2). \quad (6)$$

The amplitudes (a_i) and widths (W_i) were adjusted for a best fit. We assumed the W_i equal for Ga and As. We were able to obtain general fits comparable to the cosine corrugation but which also included the asymmetry for specific θ_i for $\phi = 0^\circ$ and 180° but we were unable to fit satisfactorily the sequence of scans of fig. 2 with one set of parameters. An interesting result for a strong corrugation was obtained by setting $a_{\text{Ga}} = 0.93 \text{ \AA}$ and $a_{\text{As}} = 1.70 \text{ \AA}$ with $W = 15 \text{ \AA}^{-2}$. This W corresponds to a half height radius of $\sim 2 \text{ \AA}$. In fig. 14 we illustrate this corrugation function $\zeta(x, y)$ for two cuts across the unit mesh ($y = 0, y = 1/2$) at $\phi = 0^\circ$ which intersect the Ga and As nuclear positions. The maximum corrugation for this function is $\sim 1.6 \text{ \AA}$. The calculated diffraction patterns are plotted in fig. 15 and the agreement

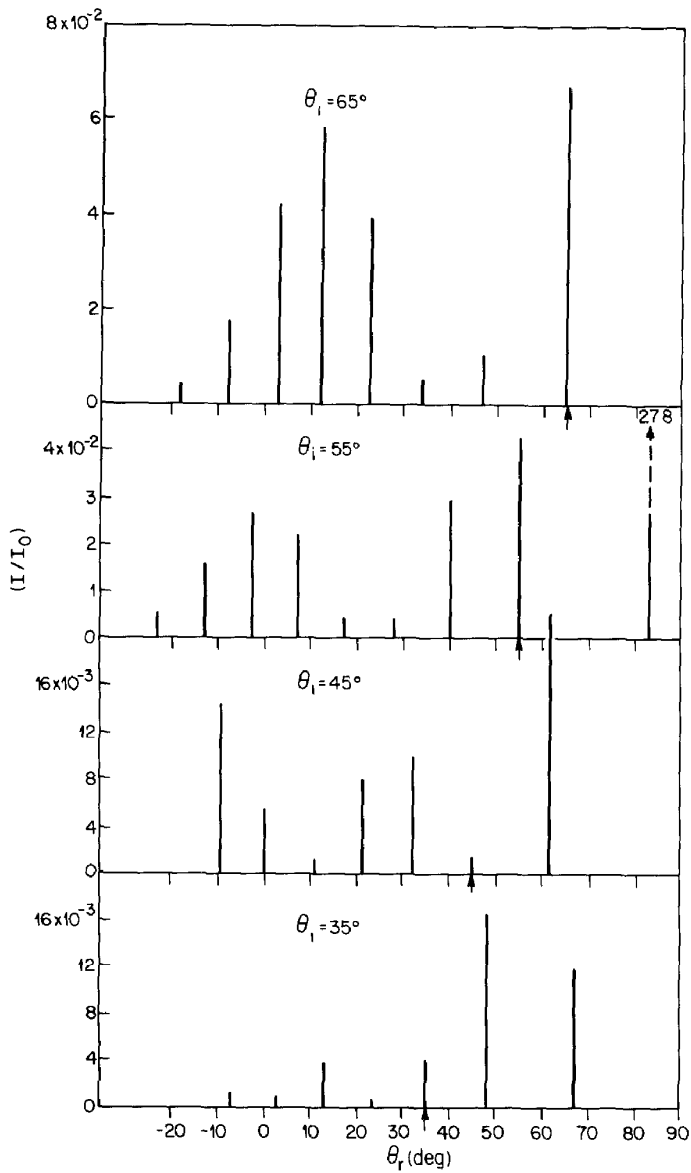


Fig. 13. Diffraction intensities calculated using the eikonal approximation for the hard wall corrugation function $\zeta(x, y) = 0.6 \cos(2\pi x/L_x) + 0.2 \cos(2\pi y/L_y)$ for a series of four incidence angles and $\lambda = 0.98 \text{ \AA}$. For comparison see the data of fig. 2.

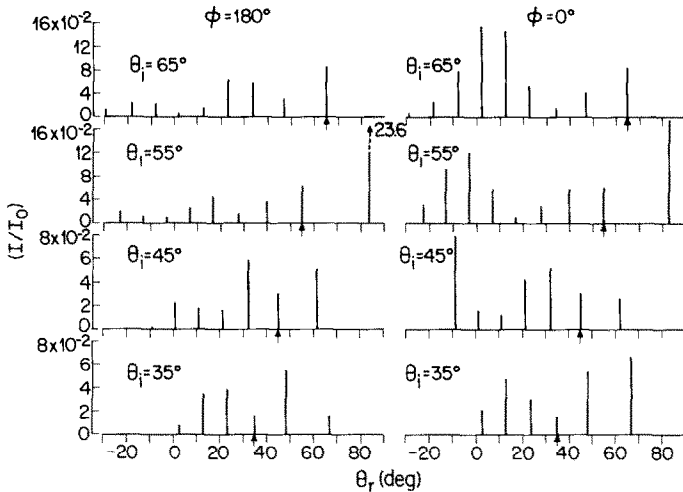


Fig. 15. Calculated diffraction intensities using the eikonal approximation for the hard wall corrugation function described in fig. 14 for $\phi = 0^\circ$ and 180° at $\lambda = 0.98 \text{ \AA}$. For comparison see the data of fig. 2.

well depth D of range greater than the corrugation is made, then

$$d_{\perp} = n\lambda' / (2 \cos \theta'_i), \quad (8)$$

where $\lambda' = \lambda(1 + D/E)^{-1/2}$ and $\theta' = \sin^{-1}[\sin \theta_i(1 + D/E)^{-1/2}]$. Note that there are three parameters; d_{\perp} , D , and n that can be adjusted to fit the features of the specular intensity envelopes.

The most consistent feature in these scans is the broad maximum occurring at $\theta_i = 24^\circ$ in all the runs of figs. 7–9. In the absence of an attractive well this corresponds to a λ_{\perp}/n of 0.54 \AA . If $n = 2$, $d_{\perp} \sim 1.1 \text{ \AA}$ in agreement with the corrugation obtained from the diffraction analysis. The $n = 1$ maximum should then occur at 63.5° . In figs. 7 and 8 there is generally a strong maximum between 65° and 70° . The inclusion of a uniform well of depth $D < 5 \text{ meV}$ is sufficient to bring this assignment ($d_{\perp} = 1.1 \text{ \AA}$) into accord with the data. Note that the interference oscillations should be more narrow at grazing angles if the widths are constant in Δk_{\perp} . Another recurrent feature of the data is a broad maximum near $\theta_i = 47^\circ$ corresponding to $d_{\perp}/n = 0.75 \text{ \AA}$. This distance does not appear in the simple cosine fit of the diffraction data. A test of this type of analysis is a series of specular scans at different wavelengths as shown in fig. 10 where a correlation of features with $\cos(\theta_i/\lambda)$ is expected. At $\lambda = 0.57 \text{ \AA}$, using $d_{\perp} = 1.0 \text{ \AA}$ and $D = 0$, we expect maxima at $\theta_i = 73^\circ$, 55° , and 31° which accounts for some of the features of the data. However, the second distance of $d_{\perp} = 0.75 \text{ \AA}$ would generate maxima at $\theta_i = 68^\circ$ and 40° for $\lambda = 0.57 \text{ \AA}$ and $\theta_i = 53^\circ$ for $\lambda = 0.90 \text{ \AA}$ which is also consistent with the

data. For $\theta_i > 70^\circ$ the effect of resonances is apparently quite strong and there is an additional strong fall-off due to the beam spreading across the crystal. At $\lambda = 0.98 \text{ \AA}$ the angle of the single envelope does not scale with $\cos(\theta/\lambda)$ as for $\lambda = 0.90 \text{ \AA}$ and $\lambda = 0.57 \text{ \AA}$. It occurs halfway between the maxima positions predicted for $d_\perp = 1.1 \text{ \AA}$ (64°) and $d_\perp = 0.75 \text{ \AA}$ (49°) for $D = 0$ as if the maxima had coalesced similar to the diffraction rainbows at grazing incidence.

An important result of the eikonal approximation is the lack of azimuthal dependence of specular scattering (see eq. (4)). A comparison of fig. 9 or fig. 10 with figs. 7 and 8 show substantial differences in the diffraction envelopes, which must reflect a strong variation in multiple scattering and/or inelastic cross section with azimuth (corrugation). Within the simple interpretation of the k_\perp interference analysis, the difference in corrugation along different azimuths appears to make the scattering sensitive to different distances. For $\lambda = 0.57 \text{ \AA}$, $d_\perp = 1.0 \text{ \AA}$ and $D = 0$, eq. (7) predicts maxima at 73° , 55° , and 31° . Note that the positions of the maxima in fig. 11 for both wavelengths are in reasonable accord despite very different intensity envelopes. Thus the maxima for $\phi = 90^\circ$, $\lambda = 0.57 \text{ \AA}$ for $\theta_i < 78^\circ$ are also fit reasonably well by two distances $d_\perp = 1.0 \text{ \AA}$ and $d_\perp = 0.75 \text{ \AA}$ for $D = 0$.

The envelopes of the specular intensity scans, analyzed using eq. (7), suggest the presence of two distances in the corrugation, $d_\perp = 1.0\text{--}1.1 \text{ \AA}$ and $d_\perp = 0.75 \text{ \AA}$ which dominate the interference patterns. The angles of the envelope maxima scale reasonably well with $\cos(\theta/\lambda)$ except for the case, $\phi = 90^\circ$, $\lambda = 0.98 \text{ \AA}$ where there may be a coalescence of the maxima. This scaling suggests the effective attractive potential depth is not large, i.e. $D \leq 5 \text{ meV}$. The strong oscillations due to surface resonances and the rapid variation of the envelopes with azimuth far from the [10] directions give rise to considerable uncertainty about the identification and indexing of the interference features. If we consider distances greater than the 1.1 \AA , which we derived from the analysis of the diffraction scans, we can obtain an interesting fit to the high energy scan of fig. 11. Using $d_\perp = 1.5 \text{ \AA}$ ($D = 0$), maxima are predicted for $n = 1\text{--}4$ at $\theta_i = 79^\circ$, 68° , 56° , and 42° . The addition of a well of depth $D = 2 \text{ meV}$ with a distance d_\perp of 1.61 \AA gives maxima at 81.5° , 68.4° , 56° , and 42° in striking agreement with the spectrum. This value of 1.6 \AA is the same corrugation height used in the diffraction calculations of fig. 15.

The eikonal theory can be used as well to analyze the structural information in the specular intensity scans. For a simple cosine corrugation the specular intensity varies as $J_0^4(c)$ where J_0 is the zeroth order Bessel function and $c = dk_\perp \cos \theta_i$. Here, d is the peak-to-peak amplitude of the corrugation function. Note that the separation of the maxima of $|J_0|$ are nearly π to within 1%. This leads to the equivalent of Bragg's law for the separation of the maxima, i.e. $dk_\perp \Delta \cos \theta = \pi$ or $2d \Delta \cos \theta = \lambda$. The first maximum occurs, however, for $c = 3.83$ which results in a discernible shift from Bragg's law. For example if $\lambda = 1 \text{ \AA}$, $d = 1 \text{ \AA}$, $n = 1$, Bragg's law gives the first maximum at $\theta_i = 60^\circ$ whereas the eikonal gives $\theta_i = 52^\circ$.

The results for the eikonal maxima for the specular scans yield distances similar to those in the Bragg analysis. For figs. 7 and 8 the maximum at 24° for $n = 2$

yields $d_{\perp} = 1.2 \text{ \AA}$ and predicts the first maximum at 60° . Again a uniform potential of depth $D < 5 \text{ meV}$ puts the $n = 1$ and 2 maxima at 60° and 24° for $d_{\perp} \sim 1.1 \text{ \AA}$. The recurrent feature at $\theta_i = 47^{\circ}$ now corresponds to $d_{\perp} = 0.88 \text{ \AA}$. In fig. 10 the maxima are predicted by the eikonal calculation for $d_{\perp} = 1.2 \text{ \AA}$ to be at 73° , 58° , and 40° for $D = 0$. A second distance of 0.86 \AA also puts $n = 1, 2$ maxima at 42° and 66° .

5. Conclusion

We have presented an extensive set of in-plane diffraction data for the scattering of He from the GaAs(110) surface. The data cover a wide range of incident polar angles at four azimuthal angles and at two wave lengths. For the same incident parameters we have recorded the specular intensity variation with polar angles for a series of azimuths.

The diffraction data as a set are characteristic of a well ordered, strongly corrugated, elastic scattering surface. Both classical scattering and the eikonal scattered wave analysis indicate that the surface is rough across the troughs and relatively smooth parallel to the troughs with respective corrugations of $\sim 1.1 \text{ \AA}$ and $\sim 0.3 \text{ \AA}$. The surface has a slight scattering asymmetry between the $[01]$ and $[0\bar{1}]$ directions which is likely due to the reconstruction rather than the atomic number difference between Ga and As.

Classical rainbow scattering analysis of the diffraction patterns is shown useful in determining the extent of the corrugation for incident angles far from grazing. The analysis requires discrimination between rainbows and supernumerary rainbows. This can be done in principal by varying the incident energy and observing if a maximum stays approximately at constant angular displacement from specular except for a minor correction for refraction. It is clearly inappropriate as the incident angle moves away from the surface normal and extrema being to coalesce. The eikonal scattering theory for a hardwall model of the surface confirms the extent of the surface corrugation derived classically and correctly predicts the supernumerary maxima for $\phi = 0^{\circ}$ and 180° at $\lambda = 0.98 \text{ \AA}$. Several of the diffraction scans could be fit qualitatively by simple cosine corrugation functions or more complex summations of Gaussian functions located above each nucleus. However, we could not find a hard wall corrugation with or without a uniform potential well attached which produced acceptable agreement over a range of incident conditions. In particular, the supernumerary oscillations at $\lambda = 0.57 \text{ \AA}$ could not be fit at all.

The envelopes of the specular intensity scans are interpreted in terms of interference in k_{\perp} using a Bragg equation (eq. (7)) and using the eikonal calculation. Both analyses gave similar results for peak-to-peak distances of the corrugation (d_{\perp}). In general, distances of $1.0\text{--}1.1$ and $0.7\text{--}0.8 \text{ \AA}$ dominate the analysis. The magnitude of the corrugation and the variation of these spectra with azimuth demonstrate that the eikonal theory and the sudden approximation [4] scattering theories are

inappropriate for detailed analysis of this surface. Within the context of the k_{\perp} interference analysis the surface appears structurally more complex than the simple cosine hard wall model suggests. The three-dimensional topography of the potential surface makes it unlikely that simple one-dimensional models we have used will fit most of the data.

An interesting note is the comparable qualitative fit to the diffraction scans we obtained using a more strongly corrugated surface with a $d = 1.6 \text{ \AA}$. This value of d also provides a good fit (k_{\perp} interference) to the high energy specular scan of fig. 11. However, the overall fit by the weaker corrugation is superior at this level of analysis.

Further refinements with the approximations we use in both the potential and scattering theory are unwarranted. It is clear that detailed geometric interpretation from atom scattering can not be made at the level of analysis employed here. More rigorous scattering calculations are required and the potential must be realistically modeled using as criteria the *simultaneous* fitting of the diffraction data over a broad range of incident conditions and the specular intensity scans including surface resonances.

Acknowledgement

The authors acknowledge R. Laughlin for numerous enlightening discussions which included preliminary results of his calculations. We thank W. Wiegmann for supplying the sample and R.A. Logan for his assistance in determining the sample orientation.

References

- [1] M.J. Cardillo and G.E. Becker, Phys. Rev. B5 (1980) 1497.
- [2] P. Cantini, G. Boato and R. Colella, Phys. Rev. Letters 42 (1979) 1635.
- [3] U. Garibaldi, A.C. Levi, R. Spadacini and G.E. Tommei, Surface Sci. 48 (1975) 649.
- [4] R.B. Gerber, A.T. Yinnon and J.N. Murrell, Chem. Phys. 31 (1978) 1.
- [5] K.H. Rieder and T. Engel, Phys. Rev. Letters 43 (1979) 373.
- [6] M.J. Cardillo and G.E. Becker, Phys. Rev. Letters 42 (1979) 508.
- [7] (a) C.B. Duke, R.J. Meyer, A. Paton, P. Mark, A. Kahn, E. So and J.L. Yeh, J. Vacuum Sci. Technol. 16 (1979) 1252.
(b) B.J. Mrstik, S.Y. Tong and M.A. Van Hove, J. Vacuum Sci. Technol. 16 (1979) 1258.
- [8] R. Laughlin, Bell Labs, to be published.
- [9] M.J. Cardillo, C. Ching, E.F. Greene and G.E. Becker, J. Vacuum Sci. Technol. 15 (1978) 473.
- [10] H.C. Gatos and M.C. Levine, in: Progress in Semiconductors, Eds. A.F. Gibson and R.E. Burgess (Temple, London, 1965).
- [11] J.L. Beeby, J. Phys. C (1971) L359.
- [12] R. Willardson and A. Beer, Eds., Semiconductors and Semimetals, Vol. 2 (Academic Press, New York, 1966) pp. 56, 171.
- [13] S.J. Sibener, M.J. Cardillo and G.E. Becker, 40th Annual Conf. on Physical Electronics, Cornell Univ. (June 1980).
- [14] E.F. Greene and E.A. Mason, Surface Sci. 75 (1978) 549.
- [15] N. Garcia, J. Chem. Phys. 67 (1977) 897.
- [16] M.J. Cardillo, Phys. Rev. 23 (1981) 1.